ADVANCED MATERIALS
www.advmat.de

Gires–Tournois Immunoassay Platform for Label-Free Bright-Field Imaging and Facile Quantification of Bioparticles

Young Jin Yoo, Joo Hwan Ko, Gil Ju Lee, Jiwon Kang, Min Seok Kim, Stefan G. Stanciu, Hyeon-Ho Jeong, Dae-Hyeong Kim, and Young Min Song**

Bright-field imaging of nanoscale bioparticles is a challenging task for optical microscopy because the light–matter interactions of bioparticles are weak on conventional surfaces due to their low refractive index and small size. Alternatively, advanced imaging techniques, including near-field microscopy and phase microscopy, have enabled visualization and quantification of the bioparticles, but they require assistance of sophisticated/customized systems and post-processing with complex established algorithms. Here, a simple and fast immunoassay device, Gires–Tournois immunoassay platform (GTIP) is presented, which provides unique color dynamics in response to optical environment changes and thus enables the label-free bright-field imaging and facile quantification of bioparticles using conventional optical microscopy. Bioparticles on GTIP slow down the velocity of reflected light, leading to vivid color change according to the local particle density and maximizing chromatic contrast for high spatial distinguishability. The particle distribution and density on the surface of the resonator are readily analyzed through 2D raster-scanning-based chromaticity analysis. GTIP offers multiscale sensing capability for target analytes that possess different refractive indices and sizes.

1. Introduction

Effective visualization and quantification of nanoscale substances are helpful techniques that photonic research can provide in the COVID-19 pandemic era caused by the SARS-CoV-2 coronavirus.[1,2] Nanoscale bioparticles with low refractive indices cause weak light–matter interactions, making them difficult to be optically observed.[3–5] To address this challenge, a variety of techniques have been used to visualize nanoparticles, viruses, and biomolecules including near-field optical microscopy,[6,7] ultra-high-resolution microscopy,[8–10] electron microscopy,[11–13] and other recently developed imaging and/or quantification techniques.[5,14–23] Although these methods provide excellent resolution and quantitative information, these conventional approaches to imaging nanoscale bioparticles require sophisticated and/or customized equipment, complex data-processing algorithms, and specialized personnel.[7,9,10,14–17,21] These prerequisites are particular limiting factors for the facile detection/quantification of bioparticles in point-of-care settings or resource-constrained settings.[24–26]

Over the past few decades, advances in optics have enabled the control of the speed of light propagating through optically dispersive media, thus presenting numerous opportunities for the utilization of light.[27] Slow light promotes strong

Y. J. Yoo, J. H. Ko, J. Kang, M. S. Kim, H.-H. Jeong, Y. M. Song
School of Electrical Engineering and Computer Science
Gwangju Institute of Science and Technology
Gwangju 61005, Republic of Korea
E-mail: ymsong@gist.ac.kr

G. J. Lee
Department of Electronics Engineering
Pusan National University
Busan 46241, Republic of Korea

The ORCID identification number(s) for the author(s) of this article can be found under https://doi.org/10.1002/adma.202110003.

DOI: 10.1002/adma.202110003

S. G. Stanciu
Center for Microscopy-Microanalysis and Information Processing
Politehnica University Bucharest
Bucharest 060042, Romania

D.-H. Kim
Center for Nanoparticle Research
Institute for Basic Science (IBS)
Seoul 08826, Republic of Korea

D.-H. Kim
School of Chemical and Biological Engineering
Institute of Chemical Processes
Seoul National University
Seoul 08826, Republic of Korea
E-mail: dkim98@snu.ac.kr

D.-H. Kim
Department of Materials Science and Engineering
Seoul National University
Seoul 08826, Republic of Korea

light–matter interactions, which can also be exploited for biosensing by allowing additional control over the spectral bandwidth.[28] Previously reported slow-light-based bio-/single-molecular platforms mainly utilized nanovolume-scale structures for the preparation of slow light, such as nanocavities in the surface-enhanced Raman scattering substrates.[29–31] Meanwhile, as a simple structure for effectively controlling light, Gires–Tournois (GT) resonators have been recently studied as flat metasurfaces including dynamic phase-change absorbers,[32] achromatic surface cloaking and lensing,[33] and colored perovskite solar cells.[34] However, despite the recent emphasis on multiscale biointerfaces design,[35] these strong designable modulators have not yet been optimized for bioimaging requiring low-index viral particle detection.

Here, we present an intuitive and robust approach for the label-free bright-field imaging and facile quantification of viral particles (VPs) using a planar metacavity designed for slow-light conditions. As a powerful and designable light-control modulator, we utilized the GT resonator for inducing slow light that promotes strong light–matter interactions.[36] By harnessing its sensitive unity absorption properties,[37] we designed a GT immunoassay platform (GTIP) for label-free imaging of SARS-CoV-2 VPs. For the non-infectious imaging test of SARS-CoV-2, we prepared VPs by decorating the surface of SiO_2 nanospheres with SARS-CoV-2 spike proteins. Local clusters formed from the VP droplets on the antibody-immobilized GTIP were detected with distinct colors from the background. From the cluster colors, particle counts could be estimated through the 2D raster-scanning-based chromaticity analysis, and the particle distribution and density could also be successfully quantized. Furthermore, during the analysis process, the slow light effect according to the cluster shape of VPs and the resulting chromaticity characteristics were derived using finite-difference time-domain (FDTD) simulations, and thus the optimal design according to various analytes could be presented. For practical applications, the air-borne droplet detection using GTIP integrated on a face protective mask was demonstrated.

2. Results and Discussion

2.1. GTIP for Bright-Field Imaging and Quantification of VPs

Figure 1 describes the proposed strategy for label-free bright-field imaging of VPs. First, we employed the GT structure, a planar resonator that can make a strong resonance without nanopatterning and can be easily applied to a large area. The proposed GT resonator has a tri-layer configuration with a porosity (P_r) of an intermediate layer to expand the design capability, which provides an optimal platform design according to the refractive index and size of the analyte (Figure 1a; Figure S1, Supporting Information for more details). By adopting the tri-layer structure, the unity absorption is achieved in a low-refractive-index medium similar to the target analyte, which is sensitive to analyte changes on its surface due to the enhanced multiple interferences by the additional resonant cavity. Visually, a large color difference with the analyte is observed, allowing a facile colorimetric detection.[38] We present an optimal design for bright-field imaging of SARS-CoV-2, in which the SARS-CoV-2 spike antibody is immobilized on the surface of the designed GTIP to specifically capture the SARS-CoV-2 spike protein (Figure 1b).

Second, as an artificial analyte that is structurally similar to SARS-CoV-2, we prepared VPs by attaching SARS-CoV-2 proteins to silica nanospheres (Figure 1c). The 100-nm silica nanospheres possess almost zero extinction through the whole visible range, with a refractive index of 1.47, which is similar to that of SARS-CoV-2 particles.[39,40] After dropping the prepared VP solution onto the antibody-bound GTIP surface, the droplets were locally dispersed by the high surface energy of the hydrophilic surface during the drying process.[41] Meanwhile, inside the droplet, VPs were vortexed by the Marangoni flow[42] (Figure 1d; Figure S2, Supporting Information for more details). The VPs initiate a cluster growth as a monolayer by recruiting other particles at the air–solution interface. After the cluster is formed, while moving following the surface fluid flow as a whole, each cluster is allowed to combine with others through a stochastic approach. VPs clusters are primarily formed from monolayers at low concentrations.[43] At relatively high concentrations, clusters can be intermittently overlapped at the droplet edge into form bi-layers[44] (Figure S3, Supporting Information). After evaporation of the droplet, the GTIP surface is rinsed in buffer solution to remove non-specific binding (Figure S4, Supporting Information).

Finally, the VP clusters on GTIP which are sensitive in photopic vision by the slow light effect were colorimetrically visualized (Figure 1e; Figure S5, Supporting Information for more details). GTIP provides visually distinct color changes when analytes are present on its surface because outgoing light from the resonator slows down while traveling through the volume populated by analytes. This is due to the local effective medium changes caused by VPs on the GTIP, which are designed to be sensitive in the low-refractive-index media and result in the change of the unity absorption condition. In the visible range, the reflectance spectra of the cluster and background area are clearly distinguished due to the shift of the resonance dip. For quantification, a stitched image of the entire sensing area was obtained by microscopic 2D scanning in a defined sensing area (Figure 1f). The chromatic information of each cluster area was extracted from the image array, and the cluster area was separated by chromaticity analysis. Particle counts were then estimated by matching simulated chromaticity results in the cluster regions. Evaluated particle counts were summed for each unit area to obtain the VP distribution over the entire sensing area. By merging the density data over the entire sensing area, the number density to estimate the concentration could be also obtained.

2.2. Optical Modeling of the GT Resonator for Colorimetric Visualization

Figure 2a illustrates a tailorable GT resonator for the colorimetric detection and visualization, based on a tri-layer configuration of SiO_2/P_r-Ge/Au. The oxide layer (SiO_2) was employed as a low-refractive-index layer to interact with low-refractive-index substances such as viruses, and the complex refractive index layer (P_r-Ge) was inserted between the low-refractive-index layer

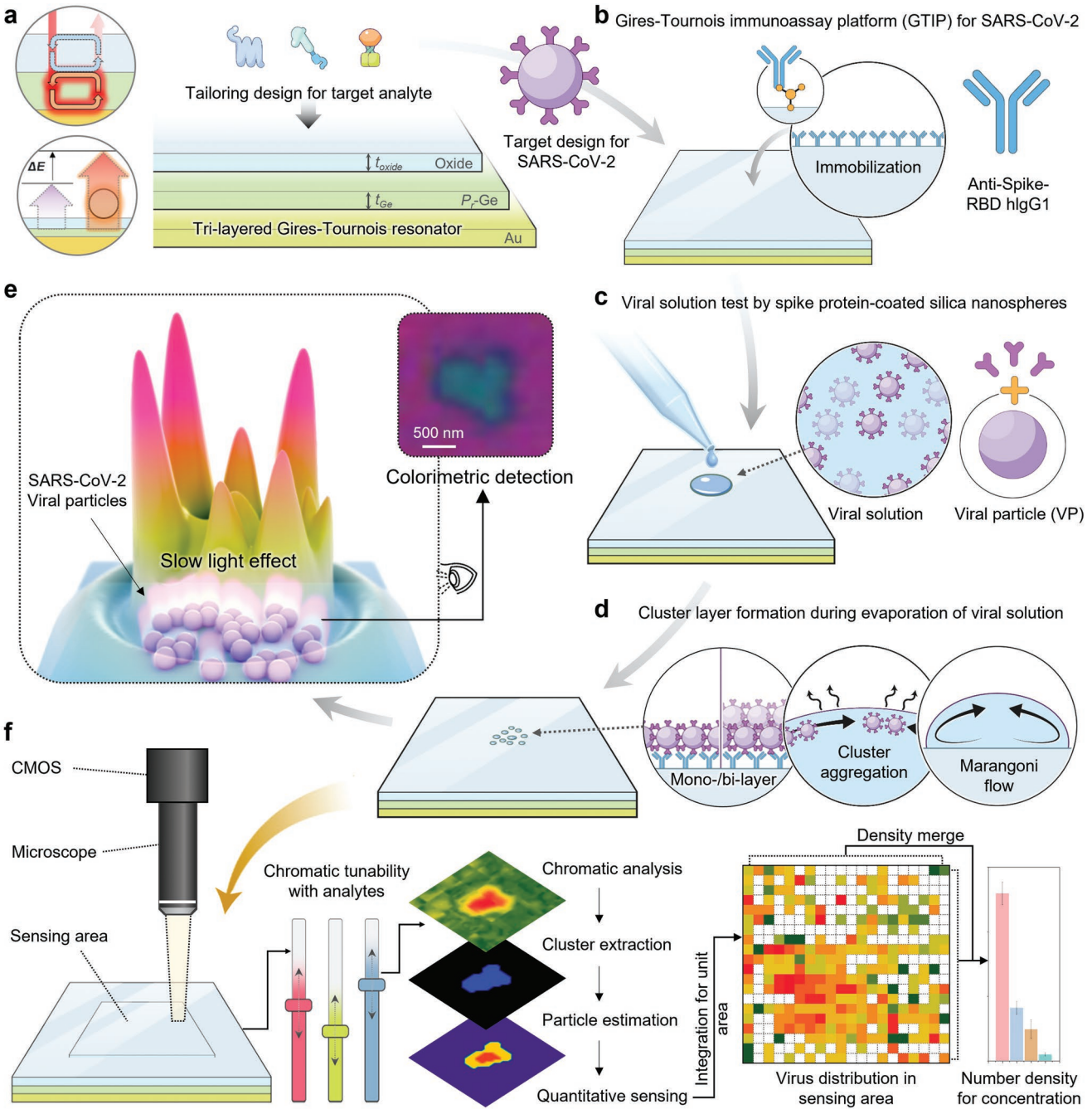

Figure 1. Gires–Tournois immunoassay platform (GTIP) for bright-field imaging and quantification of VPs. a) Schematic of the structure and properties of GTIP. b) Antibody immobilization for SARS-CoV-2 spike protein detection. c) VPs obtained by synthesizing SARS-CoV-2 and silica nanoparticles. d) Schematic illustration of the viral particle movement in the droplet by Marangoni flow. Localized cluster formation by bursting the droplets during the drying process. e) Colorimetric detection on SARS-CoV-2 particles with sensitive slow light in photopic vision. f) Cluster analysis using chromatic information for quantitative sensing.

and the metal mirror (Au) to enable the resonant behavior of the GT structure by multiple-beam interferences. Tuning three design parameters sensitively, including the thicknesses (t_{SiO2} and t_{Ge}) and P_r of the layers involved in the complex interferences, leads to a tailored design for the strong resonance with unity absorption on the low-refractive-index medium (see Note S1, Supporting Information for the detailed design process). Basically, GT structures accompany group delays (GDs) due to a nonlinear phase shift with resonant behavior. To maximize the colorimetric behavior, the target wavelength was determined in the chromatically sensitive range with the highest spectral sensitivity (Figure S6, Supporting Information). To maximize the slow-light effect, GDs of the GT resonators were calculated for three design parameters, that is., t_{SiO2}, t_{Ge}, and P_r (Figure 2b;

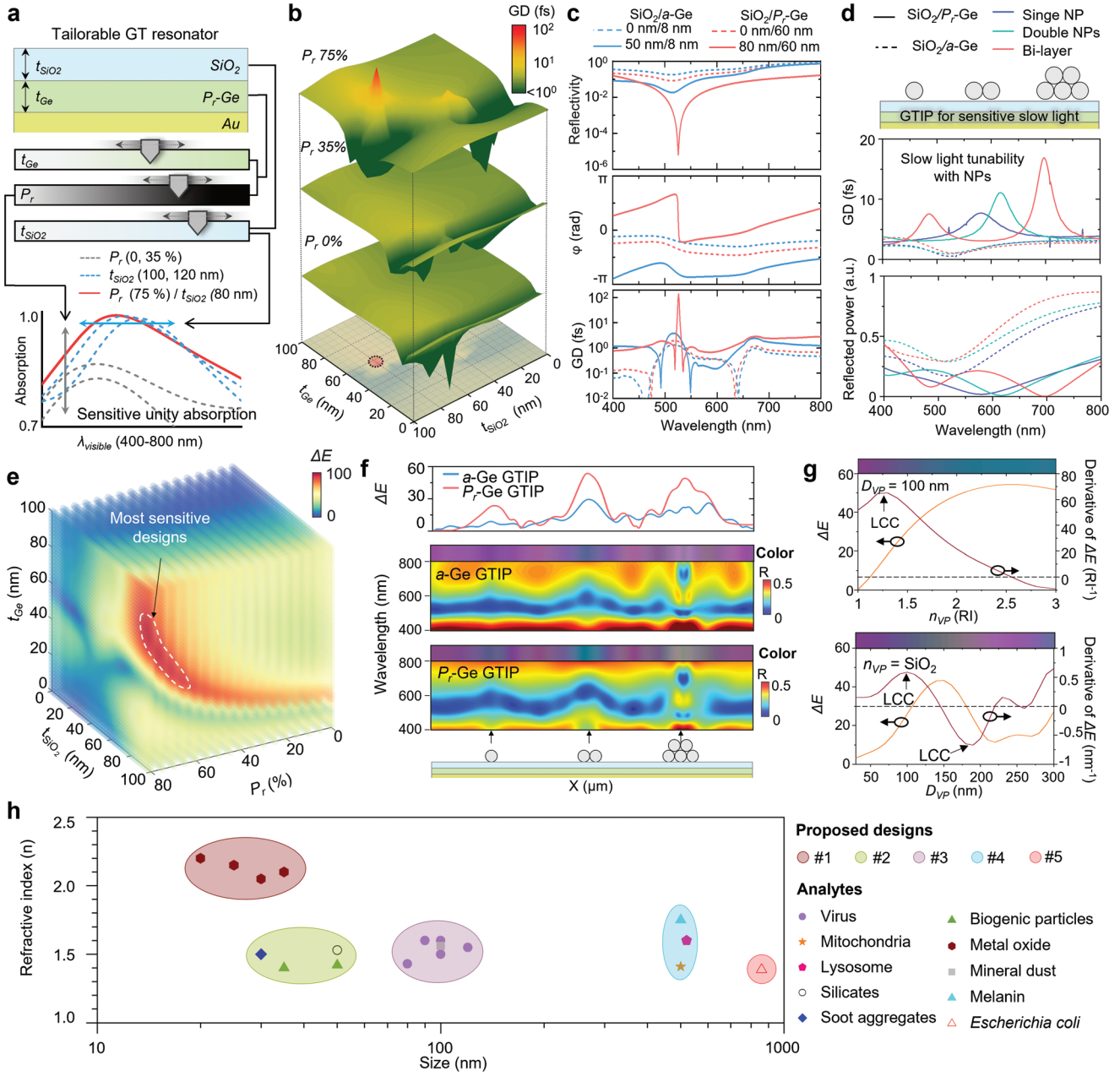

Figure 2. Optical modeling of GT resonators for colorimetric visualization. a) Schematic of the GT resonator with tunable design parameters. b) Group delay (GD) of the GT resonator with different t_{Ge}, t_{SiO2}, and P_r for sensitive slow light. c) Reflectivity, phase, and GD of four GTIPs. Dashed and solid lines indicate that the thickness of SiO_2 is 0 and 80 nm, respectively. d) Reflected power spectra and GD of GTIPs with SiO_2/a-Ge and SiO_2/P_r-Ge for different VP statuses (i.e., numbers and layers). e) Color difference (ΔE) with different t_{Ge}, t_{SiO2}, and P_r. Closed white dashed lines refer to the most sensitive designs, that is., high ΔE. f) Spatial ΔE of a-Ge GTIP and P_r-Ge GTIP. Spatial reflected power spectra (bottom) and color representation (top) of a-Ge GTIP and P_r-Ge GTIP. The illustration shows the morphologies of VPs. g) ΔE and derivatives of ΔE for P_r-Ge GTIP as a function of the refractive index of VP (n_{VP}). The diameter of VP (D_{VP}) is set to 100 nm. 'LCC' denotes a large color change. ΔE and the derivative of ΔE for P_r-Ge GTIP as a function of D_{VP}. The refractive index of SiO_2 was used for n_{VP}. h) Universality of several GTIPs for various analytes with different refractive indices and sizes.

Figure S7, Supporting Information for more details). Based on these results, we selected a GT design with a P_r of 75%, a t_{Ge} of 60 nm, and a t_{SiO2} of 80 nm, which shows the highest GD as an optimal structure for the slow-light effect.

The reflectivity spectra indicate that the P_r-Ge-based GTIP (red curves) exhibited the lower reflectivity than the amorphous Ge-based GTIP (blue curves), regardless of the SiO_2 thickness (Figure 2c; top). In particular, the presence of the SiO_2 layer leads to the significantly stronger absorption at a wavelength of 526 nm. Figure 2c (middle) illustrates the phase changes of four types of GTIPs. Although phase changes were observed at each resonant wavelength, the GTIP with SiO_2/75% P_r-Ge displayed a notable phase change of approximately π. Owing to this abrupt phase change, the GTIP with SiO_2/75% P_r-Ge

served as a strong slow-light medium at a wavelength of 526 nm (Figure 2c; bottom). Figure 2d shows GD and reflectivity of GTIPs with VPs. Spectral variation of the slow-light effect was exhibited by VPs in the P_r-Ge-based GTIP, whereas slow light was rarely observed in the amorphous Ge-based GTIP. As a result, the reflectivity spectra of the P_r-Ge-based GTIP could be clearly distinguished, depending on the VP distributions.

For colorimetric characterization using the GTIP, we calculated the color difference (ΔE) by adjusting the design parameters t_{SiO2}, t_{Ge}, and P_r (Figure 2e). The detailed simulation results and methods are shown in Figures S8–S11 and Note S2, Supporting Information. The most sensitive GTIP designs, which are marked with white dashed lines in Figure 2e, ranged from a P_r of 60–80%, a t_{SiO2} of 80–100 nm, and a t_{Ge} of 60–80 nm, including the optimal structure for slow light. Spectral and colorimetric analyses were conducted spatially by using the optimized structure (Figure 2f). The GTIP based on P_r-Ge demonstrated spatially classifiable reflected power spectra according to the number and layer of VPs; thus, a bluish green color was observed on the GTIP with a single VP and double VPs in contrast to the magenta color for the background. In the bi-layer case, the expected color was greenish grey. The GTIP based on P_r-Ge showed apparent color changes, and accordingly hue variations. The other substrates showed negligible color differences.

For universal applications of the GTIP, we calculated the color difference and the derivative of the color difference for several combinations of the design parameters of the GTIP. As expected, the previously designed GTIP structure optimized for the SARS-CoV-2 visualization exhibited a high color sensitivity (i.e., large color changes (LCCs)) for the refractive index and size of the SARS-CoV-2 VPs (Figure 2g). Different combinations of the GTIP design parameters showed color sensitivities (i.e., LCCs) in different ranges of the refractive index and size. The results indicate that oxide layers with a low P_r and a high refractive index are more suitable for the high-refractive-index analytes: P_r and oxide layers with similar refractive indices should be used to match the refractive index of the analyte, and the detailed optimization is required depending on the analyte size. The GTIP is therefore widely applicable, with potential designs suitable for analytes with various refractive indices (1.4–2.2) and sizes (10–1000 nm), including viruses, biogenic particles, and metal oxides (Figure 2h; Figure S12, Supporting Information for more details).

2.3. Particle Number Estimation by Cluster Analysis with Chromatic Information

In the proposed system, VPs are usually formed as mono- or bi-layers on the GTIP surface, given the Marangoni flow. Interestingly, mono- and bi-layers show chromatic values with completely distinct saturations in a limited hue range, depending on the gap distance (D_{gap}) between the individual VPs (**Figure 3**a). Chromaticity values divided into two groups (mono-layer and bi-layers) by chromatic analysis showed positive and negative correlations with the number of particles, according to the changes in D_{gap} (Figure 3b). Estimated values are weighted against the chromatic values of mono-/bi-layers. Bare GTIP areas show magenta, while GTIP areas covered by mono-layered VPs show bluish green, and GTIP areas covered by bi-layered VPs show greenish grey, which agree well with the predictions of the numerical simulations (Figure 3c; Figure S13, Supporting Information for comparisons with other substrates). Because mono- and bi-layered VPs show clearly distinguished colors, information of the colored areas can therefore be directly converted into the numbers of VPs. The chromaticity analysis in estimating the number of VPs is allowable for the morphological distribution observed in the target analyte (Figure S14, Supporting Information). Additionally, in the GTIP configuration for chromaticity analysis, the metallic mirror layer can be replaced with some other metals instead of Au (Figure S15, Supporting Information). This colorimetric behavior, which is attributed to multiple reflections within the GTIP, could be observed as distinct colors with a bright-field microscope, while it was rather difficult to observe with a dark-field microscope, and therefore the scattering effect was negligible (Figure S16, Supporting Information).

For VP cluster analysis, we conducted cluster extraction and particle estimation by analyzing the chromatic information of the optical microscope images matched with scanning electron microscope (SEM) images (Figure 3d,e). Cluster areas were extracted by removing the background area from the hue range obtained by comparing the calculation results with multiple images taken under the same light source and experimental setting (Figure S17, Supporting Information). Furthermore, in the chromatic analysis, mono-/bi-layer areas present clearly different saturation values, and thus the mono-/bi-layer areas could be classified in the entire cluster area. Because the particle distribution and color differences in each mono-/bi-layer area exhibit positive or negative logarithmic correlations, respectively, particle estimations could be conducted by weighting the expected number of particles per a unit pixel according to the color difference in each classified area (Figure S18, Supporting Information).

From the representative pixel distribution results according to the hue range, an overwhelming number of pixels were counted solely within a specific hue range corresponding to the background color in the entire area. In the extracted cluster area, pixels related to the particle distribution were counted over a wide hue range (Figure 3f). In the case of clusters formed with the bi-layer, most pixels were counted with various particle distributions in the mono-layer, and only some areas were counted as bi-layer pixels with relatively dense particle distributions (Figure 3g). To ensure reliability, we repeatedly performed the particle number evaluation for 50 clusters (Figure 3h). In the iterative process, we optimized the particle number estimation by analyzing clusters with various particle distributions in mono-/bi-layers (Figure 3i; Figure S19, Supporting Information for more details). The estimated number of particles for 50 clusters showed a high accuracy and a strong linear correlation with the measured number of particles obtained from SEM images (Figure 3j).

2.4. Quantitative Measurement Using the Microscope Scanning of the Entire Sensing Area

Figure 4a illustrates microscope-based scanning and chromatic decoding process for the quantitative analysis. We defined the

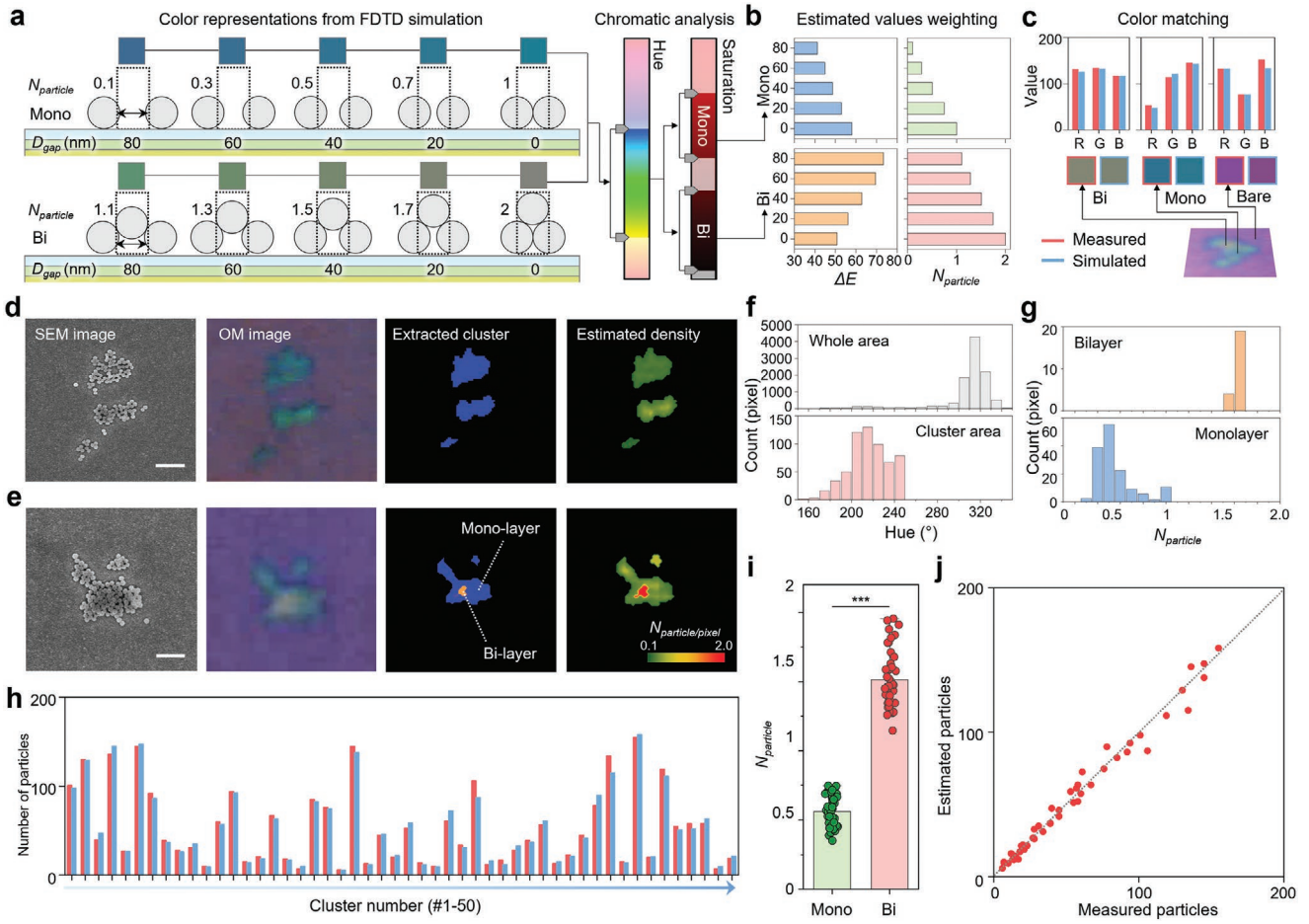

Figure 3. Particle number ($N_{particle}$) estimation by cluster analysis with chromatic information. a) Simulated colors and chromatic analysis depending on the gap distance (D_{gap}) of mono-/bi-layer VPs on GTIP. b) Estimated value weighting from color difference (ΔE) to the number of particles. c) Measured/simulated color matching of mono/bi-layers and bare cluster #1 image. d,e) SEM image, microscope image, extracted cluster, and estimated density of d) cluster #2 (mono-layer) and e) cluster #3 (bi-layer). Scale bar = 1 µm. f) Hue distributions of the entire area (top) and cluster area (bottom). g) $N_{particle}$ distributions of the bi-layer (top) and mono-layer (bottom). h) Measured (red) / estimated (blue) number of particles with different clusters. i) Averaged $N_{particle}$ of mono/bi-layers from different clusters. The data are presented as mean ± SD, $n = 50$, ***$p < 0.001$. j) Scattered dot plot of the estimated/measured particles.

sensing area (1 mm × 1 mm) through the patterning process, and dropped a controlled amount of the viral solution (300 nL; Figure S20, Supporting Information for the number of particles contained in the droplet) on the sensing area using a pump with a micro-syringe (Figures S21,S22, Supporting Information). After dropping and drying the viral solution, a stitched image array (20 × 20) covering the entire area was obtained by scanning the entire sensing area. Using a chromatic decoder optimized in the previous particle-estimation process, only color pixels in the cluster area were extracted by the elimination of the background in each pixelated image, and the particle density was derived by weighting the estimated number of particles (Figure S23, Supporting Information).

By repeating the particle counting and density integration in each unit image, the particle distribution and concentration were represented as a matrix-type heat map (Figure 4b; Figures S24–S27, Supporting Information for details). At high concentrations, particles are distributed sporadically over the whole sensing area and densely distributed in some areas. In particular, bi-layers are frequently observed in the dense areas where clusters are prone to stochastic overlap. At lower concentrations, clustered particles are locally distributed over the whole area. The densely distributed area becomes increasingly obscured, and bi-layers are rarely observable. At very low concentrations (i.e., 100 pg mL^{-1}), clusters are sparsely distributed, and both the number of cluster pixels and the estimated number of particles show low values.

Figure 4c shows the derived number of particles for each concentration, obtained through summing the number of particles over the entire sensing area (see Figure S28, Supporting Information for cluster layer distribution). The GTIP exhibits the linear detectability for SARS-CoV-2 VPs with a dynamic range of 10^2–10^6 pg mL^{-1}, and is saturated below 100 pg mL^{-1}. However, biofluids contain complex and diverse mixtures of circulating molecules that can interfere with the molecular detection. We therefore conducted a selectivity test of the GTIP using VPs of four types of analytes with various concentrations (Figure 4d), and evaluated their specific binding

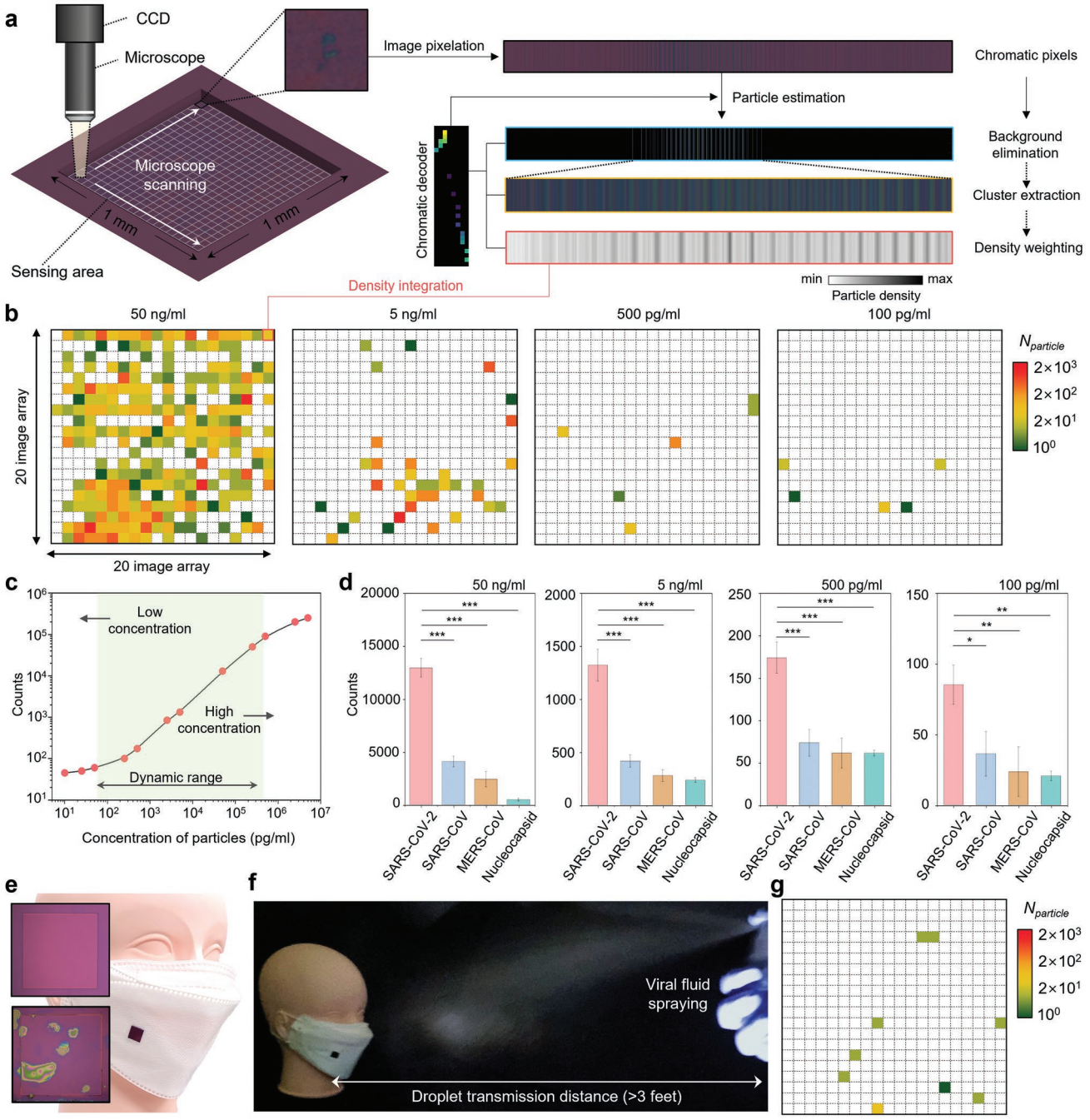

Figure 4. Quantitative measurement by microscope scanning of the entire sensing area. a) Schematic of the microscopic scanning and particle-estimation process for the entire detection area. b) Cluster distribution in the sensing area with different concentrations (i.e., 50 ng mL^{-1}, 5 ng mL^{-1}, 500 pg mL^{-1}, and 100 pg mL^{-1}). c) Cluster counts in the entire sensing area with different concentrations. d) Selectivity tests with other viral proteins were performed at each concentration. The data are presented as mean ± SD, $n = 3$, $^*p < 0.05$, $^{**}p < 0.01$, and $^{***}p < 0.001$. e) Schematic illustration of GTIP-attached face protection mask. f) Viral fluid spraying at droplet transmission distance (≈1.3 m). g) Cluster pixel distribution of the viral fluid spraying test (1 ng mL^{-1}).

behavior to the GTIP with the SARS-CoV-2 biomarker. The results show that the GTIP specifically binds to SARS-CoV-2 at similar levels from high to low concentrations. Although the GTIP shows some non-specific bindings to the analytes genetically similar with SARS-CoV-2 (e.g., SARS-CoV and MERS-CoV),[45] it shows a high selectivity to the analyte with a completely different structure such as nucleocapsids, based on immunoassay regime.

For the demonstration of practical applications of the GTIP in daily life, Figure 4e shows a GTIP-attached face mask to detect the droplet transmission by oral fluids, the main infection route of SARS-CoV-2. The GTIP surface was patterned

with sensing areas (Figure 4e top inset), and viral droplets were observed colorimetrically before evaporation due to local adsorption to the sensing area (Figure 4e bottom inset; Figure S29, Supporting Information for more details). We conducted a viral spray test using a head model wearing a GTIP mask at a distance of 3–6 feet (≈1.3 m), which is a droplet transmission distance between individuals at a high risk of infection through conversation, coughing, and laughter (Figure 4f).[46] The VP solution was sprayed at a concentration of 1 ng mL^{-1} similar to the viral copies of saliva obtained from patients.[47] Due to local adsorption of VP droplets sprayed on the detection area, the distribution and expected number of particles in the detection area could be measured (Figure 4g).

3. Conclusion

By applying the GTIP to a typical bright-field microscopic imaging procedure, we demonstrated that the VP cluster distribution and density can be determined in one-shot color images by using the systematically classified pre-simulated chromaticity data set. This strategy can have important implications in terms of presenting a simple but powerful alternative to previously-reported imaging and quantification methods using separate fluorescent or plasmonic labels (Table S1, Supporting Information). Meanwhile, to determine the presence of single nanoparticles and viruses, ultrasensitive detectors are necessary such as evanescent biosensors based on optical resonators[48] and nanowaveguides,[49] on the other hand, our technique does not transcend the optical diffraction limit to increase the spatial resolution. Thus, it cannot replace ultrahigh-resolution microscopic techniques but instead can significantly improve the chromatic contrast in the bright-field bio-imaging that enables the quantification of nanoparticles over a large sensing area. Moreover, compared to existing SARS-CoV-2 diagnostic methods, the proposed method enables a rapid detection of SARS-CoV-2 without extra sample treatments, such as amplification and labeling. The GTIP also enables more intuitive colorimetric detection than electrochemical-based methods by immobilizing single antibodies to the surface without complex immune bindings (Table S2, Supporting Information).

In more detail, the GTIP provides following advantages over conventional approaches. First, no specialized devices are required to perform GTIP experiments. Its optical design allows for the color change to be observed with a standard bright-field microscope available in most laboratories after simply placing the analyte on the surface of the GTIP. Second, the GTIP enables the selective and diverse analyte detection from a single experiment. By applying different specific target antibodies to an array of multiple sensing areas, the repetitive detection process for different analytes is eliminated. Third, the immune-binding is not the only route for the detection of analytes in the GTIP. As long as any binding agents can be attached to the surface, the GTIP can provide the amplified light–matter interactions with the analyte. Lastly, the proposed analytical strategy may be applied to the fluid dynamic monitoring of analytes with concentrations of analytical particles sprayed in air or dispersed in various forms on surfaces.

As with existing techniques for profiling single particles or particle clusters, chromatic data from GTIP are still sparse. As a caveat, since the binding of GTIP is based on a well-known immunoassay, the possibility of non-specific binding of similar structures or completely different components in addition to the target analyte cannot be completely excluded. We aim to improve this issue in the future by developing a number of differently designed assay arrays. In addition, a fully automated microscope scan setup and advanced chromaticity analysis algorithms such as deep learning may also reduce analysis time, and customized mobile phone microscopy with a dedicated app would also allow the GTIP to be easily used as a self-diagnosis kit for general users.[50] Despite current limitations, the GTIP still works as an invaluable tool for imaging viral analytes and quantifying their density in air (i.e., concentration in droplet). We further envision that the GTIP holds great potential for multiscale imaging of analytes with various refractive indices and sizes, without special treatments.

4. Experimental Section

Fabrication of the GTIP: The GTIP was prepared in two steps by: i) producing porous resonant optical layers and ii) functionalizing the surface with antibodies. First, to classify the sensing area, photolithography and etching were performed on a single-side polished silicon (100) wafer (used as a supporting substrate). An array of squares (1 cm^2) was patterned with positive photoresist (AZ 5214), and the remaining part was etched to depths of 700 nm using reactive ion etching (PLASMALAB 80 PLUS, Oxford, USA). Thin film layers of Au reflector and P_r-Ge were sequentially deposited on the patterned area by electron beam evaporation (KVE-E2000, Korea Vacuum Tech Co., Korea) under high vacuum conditions (≈10^{-6} Torr). Au was evaporated at an angle normal to the surface, and the P_r-Ge layer was deposited after mounting the substrate on a tilted sample holder at 70°. The substrate was flipped to form a uniform surface at half of the target thickness (60 nm). Sequentially, an 80-nm SiO_2 passivation layer was deposited by plasma-enhanced chemical vapor deposition (System 100, Oxford, USA). As a second step, oxygen plasma treatment was performed for 10 min to activate the surface by forming a hydroxyl group. The plasma treated substrate was then immediately soaked in 5% polyethylene glycol (PEG) 400 solution (w/w in 95% tetrahydrofuran) for 30 min. Subsequently, samples were dried at 80 °C for 20 min. The PEG-coated surface was immobilized by immersing in 100 µg mL^{-1} IgG (Anti-Spike-RBD-hIgG1, InvivoGen, USA) for 30 min at room temperature. To avoid nonspecific interactions, this PEG-IgG surface was incubated with 1% bovine serum albumin (BSA) solution 20 mg mL^{-1} (BSA solution, Biosesang, Korea) at room temperature for 20 min.

Synthesis Process of VPs: 1 mg mL^{-1} colloidal solution of silica nanoparticles (100 nm in diameter, Sigma Aldrich) was centrifuged and washed with ethanol (0.3 mL) and MilliQ water (1 mL) three times. The nanoparticles were then dispersed in 50 µL of 1% 3-aminopropyl triethoxysilane (APTES 99%, Sigma Aldrich) in 99% ethanol to cover their surface with amino functional groups overnight at room temperature. After washing with ethanol and water, the particles were immersed in a 10% glutaraldehyde solution (diluted with 50 mM PBS) and stored for 3 h, followed by antigen (50 µg mL^{-1}) injection (Spike-RBD-His, InvivoGen, USA), and then stored overnight at 4 °C.

Quantitative Test of VPs Functionalized with SARS-CoV-2: VP solutions were diluted in PBS at different concentrations (100 pg mL^{-1}–500 ng mL^{-1}). Each solution (300 nL in volume) was injected into each sensing area of the GTIP via a gastight micro-syringe (Legato 210, KD scientific Inc., USA). After evaporation of the solution,

GTIP was rinsed with PBS solution for 30 s and with DI water for 10 s to remove non-specific binding.

Optical Analysis (Bright-Field Imaging and Stitching): Optical bright-field images were acquired a 100× objectives lens (MPlanFLN, Olympus, Japan) using a CMOS camera (STC-MCCM200U3V, OMRON SENTECH, Kanagawa, Japan) with a maximum frame rate of 35.8 fps. Under a white LED lamp as a continuous light source, the exposure time required to acquire a single image was 27.5 ms. The imaging field of view was 169 μm × 141.4 μm in a single image acquisition. A motorized scanning stage with a maximum travel speed of 50 mm s^{-1} was used to scan the sensing area. To scan the sensing area, a motorized scanning stage with a maximum travel speed of 50 mm s^{-1} was used. Given the exposure time and travel speed, raster scanning over an entire area defined as 1 mm × 1 mm took about 12 s at full speed with 20 × 20 shots at 50-μm intervals. The acquired images over the entire sensing area were stitched using an automated algorithm in the software MATLAB (MathWorks, USA).

Optical Calculation: FDTD in the commercial software (FullWAVE, RSoft Design Group, USA) was used to calculate the amplitude and phase of the reflected light from the CAD-modeled GTIP. In this simulation, perfectly matched layer domains were used in the *x*/*y*/*z* directions, and the grid size was set to 5 nm for high accuracy. In addition, to obtain accurate output, material dispersions and extinction coefficients were considered. The custom-designed code using MATLAB (MathWorks, USA) was also used to calculate both the effective complex refractive indices based on volume averaging theory, and the chromatic information from the reflectance.

Statistical Analysis: All data were presented as mean ± SD and analyzed using one-way analysis of variance and Tukey's post hoc tests. Statistical significance was determined as NS (not significant, $p > 0.05$), * ($p < 0.05$), ** ($p < 0.01$), and *** ($p < 0.001$).

Supporting Information

Supporting Information is available from the Wiley Online Library or from the author.

Acknowledgements

This work was supported by the GIST Research Institute (GRI) through a grant funded by the GIST and National Research Foundation of Korea (NRF) funded by the Ministry of Science and ICT (NRF-2021M3H4A1A04086552, NRF-2017M3D1A1039288, and NRF-2021R1A4A2001827). This work was also supported by the Institute for Basic Science (IBS-R006-A1). S.G.S. acknowledges the financial support of UEFISCDI Grant RO-NO-2019-0601 MEDYCONAI. Y.J.Y. acknowledges the support from the NRF (NRF-2021R1C1C2013475). J.H.K. acknowledges the support from the NRF (NRF-2021R1A6A3A13043651).

Conflict of Interest

The authors declare no conflict of interest.

Author Contributions

Y.J.Y. and J.H.K. contributed equally to this work. Y.J.Y., J.H.K., G.J.L., J.K., M.S.K., S.G.S., H.-H.J., D.-H.K., and Y.M.S. conceived experiments. Y.J.Y., J.H.K., and J.K. developed the process and fabricated the samples. Y.J.Y., J.H.K., J.K., and M.S.K. performed experiments and characterizations of the fabricated samples with analytes. Y.J.Y., J.H.K., and G.J.L. performed theoretical analysis and optical calculations. Y.J.Y., J.H.K., G.J.L., S.G.S., H.-H.J., D.-H.K., and Y.M.S. wrote the paper.

Data Availability Statement

The data that support the findings of this study are available from the corresponding author upon reasonable request.

Keywords

bright-field imaging, chromatic analysis, colorimetric detection, Gires-Tournois (GT) resonator, particle quantification

Received: December 8, 2021
Revised: March 7, 2022
Published online:

[1] *Nat. Photonics* **2020**, *14*, 337.
[2] R. Won, *Nat. Photonics* **2020**, *14*, 271.
[3] Y.-C. Li, H.-B. Xin, H.-X. Lei, L.-L. Liu, Y.-Z. Li, Y. Zhang, B.-J. Li, *Light: Sci. Appl.* **2016**, *5*, e16176.
[4] L. He, Ş. K. Özdemir, J. Zhu, W. Kim, L. Yang, *Nat. Nanotechnol.* **2011**, *6*, 428.
[5] O. Mudanyali, E. McLeod, W. Luo, A. Greenbaum, A. F. Coskun, Y. Hennequin, C. P. Allier, A. Ozcan, *Nat. Photonics* **2013**, *7*, 247.
[6] E. Betzig, R. J. Chichester, *Science* **1993**, *262*, 1422.
[7] K. Frischwasser, K. Cohen, J. Kher-Alden, S. Dolev, S. Tsesses, G. Bartal, *Nat. Photonics* **2021**, *15*, 442.
[8] B. Huang, H. Babcock, X. Zhuang, *Cell* **2010**, *143*, 1047.
[9] B. Yang, G. Chen, A. Ghafoor, Y. Zhang, Y. Zhang, Y. Zhang, Y. Luo, J. Yang, V. Sandoghdar, J. Aizpurua, *Nat. Photonics* **2020**, *14*, 693.
[10] L. Gong, W. Zheng, Y. Ma, Z. Huang, *Nat. Photonics* **2020**, *14*, 115.
[11] S. M. Feinstone, A. Z. Kapikian, R. H. Purcell, *Science* **1973**, *182*, 1026.
[12] L. F. PeaseIII, D. I. Lipin, D. H. Tsai, M. R. Zachariah, L. H. Lua, M. J. Tarlov, A. P. Middelberg, *Biotechnol. Bioeng.* **2009**, *102*, 845.
[13] M. M. Van Schooneveld, A. Gloter, O. Stephan, L. F. Zagonel, R. Koole, A. Meijerink, W. J. Mulder, F. M. De Groot, *Nat. Nanotechnol.* **2010**, *5*, 538.
[14] C. W. Freudiger, W. Min, G. R. Holtom, B. Xu, M. Dantus, X. S. Xie, *Nat. Photonics* **2011**, *5*, 103.
[15] N. C. Lindquist, C. D. L. de Albuquerque, R. G. Sobral-Filho, I. Paci, A. G. Brolo, *Nat. Nanotechnol.* **2019**, *14*, 981.
[16] K. D. Heylman, N. Thakkar, E. H. Horak, S. C. Quillin, C. Cherqui, K. A. Knapper, D. J. Masiello, R. H. Goldsmith, *Nat. Photonics* **2016**, *10*, 788.
[17] T. Gorkhover, A. Ulmer, K. Ferguson, M. Bucher, F. R. Maia, J. Bielecki, T. Ekeberg, M. F. Hantke, B. J. Daurer, C. Nettelblad, *Nat. Photonics* **2018**, *12*, 150.
[18] F. Yesilkoy, E. R. Arvelo, Y. Jahani, M. Liu, A. Tittl, V. Cevher, Y. Kivshar, H. Altug, *Nat. Photonics* **2019**, *13*, 390.
[19] E. Balaur, G. A. Cadenazzi, N. Anthony, A. Spurling, E. Hanssen, J. Orian, K. A. Nugent, B. S. Parker, B. Abbey, *Nat. Photonics* **2021**, *15*, 222.
[20] E. Balaur, S. O'Toole, A. J. Spurling, G. B. Mann, B. Yeo, K. Harvey, C. Sadatnajafi, E. Hanssen, J. Orian, K. A. Nugent, *Nature* **2021**, *598*, 65.
[21] N. Mauranyapin, L. Madsen, M. Taylor, M. Waleed, W. Bowen, *Nat. Photonics* **2017**, *11*, 477.
[22] X. Zhou, P. Cao, Y. Zhu, W. Lu, N. Gu, C. Mao, *Nat. Mater.* **2015**, *14*, 1058.
[23] M. Lucidi, M. Marsan, F. Pudda, M. Pirolo, E. Frangipani, P. Visca, G. Cincotti, *Biomed. Opt. Express* **2019**, *10*, 5600.
[24] H. Zhu, S. O. Isikman, O. Mudanyali, A. Greenbaum, A. Ozcan, *Lab Chip* **2013**, *13*, 51.

[25] M. Zarei, *TrAC, Trends Anal. Chem.* **2017**, *91*, 26.
[26] R. M. Torrente-Rodríguez, H. Lukas, J. Tu, J. Min, Y. Yang, C. Xu, H. B. Rossiter, W. Gao, *Matter* **2020**, *3*, 1981.
[27] T. F. Krauss, *Nat. Photonics* **2008**, *2*, 448.
[28] K. L. Tsakmakidis, O. Hess, R. W. Boyd, X. Zhang, *Science* **2017**, *358*, eaan5196.
[29] Y. Lu, G. L. Liu, J. Kim, Y. X. Mejia, L. P. Lee, *Nano Lett.* **2005**, *5*, 119.
[30] R. Chikkaraddy, B. De Nijs, F. Benz, S. J. Barrow, O. A. Scherman, E. Rosta, A. Demetriadou, P. Fox, O. Hess, J. J. Baumberg, *Nature* **2016**, *535*, 127.
[31] F. Benz, M. K. Schmidt, A. Dreismann, R. Chikkaraddy, Y. Zhang, A. Demetriadou, C. Carnegie, H. Ohadi, B. De Nijs, R. Esteban, *Science* **2016**, *354*, 726.
[32] S.-J. Kim, H. Yun, S. Choi, J.-G. Yun, K. Park, S. J. Jeong, S.-Y. Lee, Y. Lee, J. Sung, C. Choi, *Nanophotonics* **2021**, *10*, 713.
[33] Y. Huang, M. Pu, F. Zhang, J. Luo, X. Li, X. Ma, X. Luo, *Adv. Opt. Mater.* **2019**, *7*, 1801480.
[34] D. Liu, L. Wang, Q. Cui, L. J. Guo, *Adv. Sci.* **2018**, *5*, 1800836.
[35] Y. Jiang, X. Li, B. Liu, J. Yi, Y. Fang, F. Shi, X. Gao, E. Sudzilovsky, R. Parameswaran, K. Koehler, *Nat. Biomed. Eng.* **2018**, *2*, 508.
[36] F. Gires, P. Tournois, *C. R. Hebd. Seances Acad. Sci.* **1964**, *258*, 6112.
[37] J. Park, S. J. Kim, M. L. Brongersma, *Opt. Lett.* **2015**, *40*, 1960.
[38] J. Du, B. Zhu, X. Chen, *Small* **2013**, *9*, 4104.
[39] H. Yao, Y. Song, Y. Chen, N. Wu, J. Xu, C. Sun, J. Zhang, T. Weng, Z. Zhang, Z. Wu, *Cell* **2020**, *183*, 730.
[40] L. Ma, S. Zhu, Y. Tian, W. Zhang, S. Wang, C. Chen, L. Wu, X. Yan, *Angew. Chem., Int. Ed.* **2016**, *55*, 10239.
[41] L. Keiser, H. Bense, P. Colinet, J. Bico, E. Reyssat, *Phys. Rev. Lett.* **2017**, *118*, 074504.
[42] W. Zhang, T. Yu, L. Liao, Z. Cao, *AIP Adv.* **2013**, *3*, 102109.
[43] K. N. Al-Milaji, R. R. Secondo, T. N. Ng, N. Kinsey, H. Zhao, *Adv. Mater. Interfaces* **2018**, *5*, 1701561.
[44] T. Xu, M. L. Lam, T.-H. Chen, *Sci. Rep.* **2017**, *7*, 1.
[45] D. Wrapp, N. Wang, K. S. Corbett, J. A. Goldsmith, C.-L. Hsieh, O. Abiona, B. S. Graham, J. S. McLellan, *Science* **2020**, *367*, 1260.
[46] P. Bahl, C. Doolan, C. de Silva, A. A. Chughtai, L. Bourouiba, C. R. MacIntyre, *J. Infect. Dis.* **2020**, jiaa189.
[47] V. Stadnytskyi, C. E. Bax, A. Bax, P. Anfinrud, *Proc. Natl. Acad. Sci. U. S. A.* **2020**, *117*, 11875.
[48] Y. Zhi, X. C. Yu, Q. Gong, L. Yang, Y. F. Xiao, *Adv. Mater.* **2017**, *29*, 1604920.
[49] M. Jin, S.-J. Tang, J.-H. Chen, X.-C. Yu, H. Shu, Y. Tao, A. K. Chen, Q. Gong, X. Wang, Y.-F. Xiao, *Nat. Commun.* **2021**, *12*, 1.
[50] P. Fozouni, S. Son, M. D. de León Derby, G. J. Knott, C. N. Gray, M. V. D'Ambrosio, C. Zhao, N. A. Switz, G. R. Kumar, S. I. Stephens, *Cell* **2021**, *184*, 323.